Acta Materialia 121 (2016) 164–172

Contents lists available at ScienceDirect

Acta Materialia

journal homepage: www.elsevier.com/locate/actamat

Full length article

Decoupling the contributions of constituent layers to the strength and ductility of a multi-layered steel

Moo-Young Seok [a], Jung-A Lee [a], Dong-Hyun Lee [a], Upadrasta Ramamurty [b], Shoichi Nambu [c, **], Toshihiko Koseki [c], Jae-il Jang [a, *]

[a] Division of Materials Science and Engineering, Hanyang University, Seoul 133-791, Republic of Korea
[b] Department of Materials Engineering, Indian Institute of Science, Bangalore 560012, India
[c] Department of Materials Engineering, The University of Tokyo, Tokyo 113-8656, Japan

ARTICLE INFO

Article history:
Received 3 June 2016
Received in revised form
2 September 2016
Accepted 5 September 2016

Keywords:
Multi-layered steel
Nanoindentation
Tensile strength
Ductility
Martensitic phase transformation

ABSTRACT

Multi-layered steel (MLS) consisting of alternating soft/ductile austenitic and hard/brittle martensitic stainless steel layers is a new class of hybrid material for structural application as it offers excellent combinations of strength and ductility. In this study, the contributions of each of the constituent layers to the overall strength and ductility of an MLS (having tensile strength > 1.4 GPa and ductility > 20%) were examined by recourse to nanoindentation experiments on each of them. By adapting two different indenter tip radii for the spherical nanoindentation experiments, constituent layers' stress-strain responses within the plastic regime were obtained and then compared with the macroscopic flow curve of the MLS that was obtained through tensile tests, to show that the strength contributions of the constituent steels to the global strength of MLS is as per the rule of mixtures. In order to examine the sources of tensile ductility of the MLS, sharp tip nanoindentation experiments were conducted on specimens extracted from tensile coupons that were subjected to predetermined plastic strains *a priori*. Results of these experiments show that the tensile failure occurs at a strain at which hardness of the austenitic layer, which is found to be dependent on the prior-plastic strain, is almost equal to the strain-independent hardness of the martensitic layer. The results are discussed in terms of martensitic transformation within austenitic layer and the role of the mechanical environment change imposed by the neighboring martensite layers on it.

1. Introduction

Steels occupy the preeminent position in the structural materials category, and considerable efforts are continually being made to enhance their mechanical performance without compromising on the inherent advantages they offer, such as the low cost, wide availability, and amenability to high volume manufacturing operations such as stamping. These efforts led to the development of a variety of advanced high strength steels (so-called AHSS) such as dual phase (DP), complex phase (CP), transformation-induced plasticity (TRIP), and twinning-induced plasticity (TWIP) steels. The microstructures of these steels consist two or more constituent phases, whose morphology and volume fractions are optimized such that enhanced combinations of high strength and ductility are available in the same material. Such steels are especially essential for environment-friendly automobiles whose structural integrity is maximum. This field of research, however, appears to have matured with further advances only leading to marginal benefits. One way of alleviating this is through the hybrid materials approach wherein two or more distinct steels are combined so as to obtain a material with far superior properties than the constituents. Such a "disruptive technology" concept has been employed to manufacture a multi-layered steel (MLS) that consists of alternating layers of hard, but relatively less-ductile martensitic stainless steel and soft, but ductile austenitic stainless steel. It was demonstrated that such a material can be extremely strong (tensile strength in excess of 1.2 GPa) and at the same time considerably ductile (at least 15% failure strain). Such strength-ductility combination is way beyond the reported trade-off between these properties in conventional

* Corresponding author.
** Corresponding author.
E-mail addresses: nambu@metall.t.u-tokyo.ac.jp (S. Nambu), jijang@hanyang.ac.kr (J.-i. Jang).

http://dx.doi.org/10.1016/j.actamat.2016.09.007
1359-6454/

steels [1,2]. Further, this MLS is reported to also exhibit high impact and bending strengths, and good formability [1,3].

While the macroscopic mechanical properties of the MLS are indeed impressive, a detailed knowledge about the role played by each of the constituent layer materials is not well known yet. Such knowledge would help in the design of even better MLS. However, it appears that the conventional reasoning, which is obtained on the basis of theoretical and experimental studies on composites, may not hold good in the case of MLS as the composites typically combine two dissimilar materials. For example, the tensile ductility of multi-layered metal composites, wherein the constituents' ductility varies significantly, is often much lower than that estimated by the rule of mixtures, if the ductility of each layer is largely different [4]. In the case of MLS, however, significant global ductility is observed in spite of the fact that the austenitic and the martensitic stainless steels exhibit vastly different tensile failure strains.

In trying to deconvolute the contributions of the constituent layers to the overall properties of the MLS, it is important to keep in mind that in addition to the nature of the materials that make them up, the interlayer interfaces can also play a dominant role, especially in determining ductility. This is especially so because a weak interface can decrease the tensile ductility through interfacial cracking or delamination [4,5]. In a recently developed MLS consisting of martensitic and austenitic stainless steel layers [1,6], such a detrimental influence of the interfaces appears to have been minimized since the MLS shows sufficiently high bond strength of the interlayer interfaces, implying, in turn, that the interfaces allow for an uniform plastic deformation of the steel. Therefore, it is the constituent layers rather than the interfaces between them that play the main role in determining the mechanical characteristics of the MLS.

Since MLS is generally fabricated by the roll bonding of stacked steel plates [1], the fractions and compositions of the hard and soft layers can be designed independently. Thus, a detailed knowledge about the contribution of each constituent layer to the macroscopic mechanical response is crucial for achieving the desired combination of an extremely high strength and ductility of MLS. However, such studies have not been reported hitherto. Although tensile tests on the monolithic specimens of the constituent materials can be performed independently (as done in Ref. [7]), the mechanical behavior of the monolithic sample cannot be the same as that of the layer in MLS due to the absence of the neighboring layers and thus stress and strain partitioning in the monolithic sample [8–10]. A promising technique to overcome this difficulty and to measure the mechanical properties of each layer is nanoindentation, which has been widely used to probe local properties of a specific phase in a variety of steels [11–16]. In the present study, we employ it to explore the contributions of each constituent layer to the macroscopic tensile properties of a MLS (consisting of the 15 alternating layers of 301 and 420 stainless steels) through a series of nanoindentation experiments with both spherical and pyramidal indenters. How the global strength and ductility of the MLS are determined is systematically examined with the support of the interrupted tensile tests and the analysis of strain-induced martensitic transformation.

2. Material and experiments

The examined MLS is composed of 15 alternating layers of SS420 grade martensitic stainless steel and SS301 grade austenitic stainless steel, with the latter being the top layer on both the sheet faces. Here afterwards, the constituent steels will be denoted simply as 301 and 420. Their chemical compositions are listed in Table 1. The initial total thickness of the MLS was 15 mm (with each layer being 1 mm thick). It was reduced to 1.2 mm by hot-rolling at 1473 K followed by cold-rolling. The final layer thickness was close to 80 μm. The sheet was then heat-treated at 1273 K for 120 s and quenched by N_2 gas.

The MLS sheet, thus produced, was electro-discharge-machined into dog-bone shaped tensile specimens with a gauge length of 20 mm. Uniaxial stress-strain (σ-ε) responses of these were measured in an universal testing machine, Z100 (Zwick GmbH & Co., Ulm, Germany). For nanoindentation, the cross-sectional surfaces of the sheet were first mechanically polished with fine SiC paper with grit number of up to 2000, and then electrolytically polished using a Lectropol-5 instrument (Struers, Westlake, OH) in a solution (ethanol 80%, distilled water 14%, perchloric acid 6%) to avoid possible artifacts related to a hardened surface layer introduced during grinding. Nanoindentation tests were carried out using a Nanoindenter-XP (formerly MTS; now Keysight, Santa Rosa, CA, USA) with three different indenters including a three-sided pyramidal Berkovich tip and two spherical tips having different radii, R, of 3.34 and 5.97 μm. The values of R were determined by analyzing the data obtained through indentations on a fused quartz sample and the Hertzian contact theory [17]. More than 30 indentation tests were made for each testing condition in order to ensure the fidelity of the results.

Microstructural observations were conducted using both optical microscopy (OM; CK40M, Olympus, Tokyo, Japan) and scanning electron microscopy (SEM; JSM-6330F, JEOL Ltd., Tokyo, Japan). For the observations, the electro-polished sample (prepared in the same way as used for nanoindentation) was electrolytically etched in the same solution as one used for electro-polishing.

The strain-induced austenite to martensite phase transformation, which occurs during tensile straining of the austenitic phase, in specimens that were subjected to a predetermined plastic strain was characterized by employing three different methods. First, the macroscopic martensite fraction was examined by employing the magnetic induction method using a Feritscope MP30 device (Helmut Fischer Gmbh, Düsseldorf, Germany). Details of this method can be found in Refs. [18,19]. Second, X-ray diffraction (XRD) analysis was performed using a D/MAX-2500 (Rigaku-Denki, Japan) diffractometer with Cu anode (wavelength $K_\alpha = 1.54184$ Å). Third, electron back scattered diffraction (EBSD) analysis was carried out in a scanning electron microscope (SU-40 and Hikari EBSD Detector, Oxford INCA, UK). The electro-polished samples were inspected at a tilt angle of 70°, and acquired data were evaluated by Orientation Imaging Microscopy (OIM) software.

3. Strength contributions

Representative optical micrograph of the cross section of the MLS is displayed in Fig. 1a. A higher magnification SEM image of the interface is shown in Fig. 1b, which indicates to a well-bonded interface between the layers. As recently reported by Nambu et al. [6] who conducted a detailed study to evaluate the interfacial fracture toughness of the layers in a different MLS, this type of well-bonded interface has a sufficiently high toughness and hence will be prevented from possible delamination failure. Inset of Fig. 2 shows a schematic of the MLS structure and the designed tensile

Table 1
Chemical compositions of the constituent layer materials (in wt.%).

	C	Si	Mn	Ni	Cr
SS420 (M)	0.29	0.61	0.44	0.22	13.13
SS301 (A)	0.10	0.51	0.78	6.54	16.80

loading direction. Fig. 2 displays representative true stress vs. true strain responses of the laminate, which are obtained by converting the measured engineering stress vs. engineering strain curves (also shown in the figure) using standard procedures. The values of ultimate tensile strength and failure strain (from engineering stress-strain curve) are 1420 ± 2 MPa and 21.9 ± 2.3%, respectively.

Since the tensile loading direction is parallel to the layers (see the schematic of Fig. 2), it is reasonable to assume that the iso-strain conditions, i.e., the strain in each of the constituent layer is the same as the global tensile strain, ε, prevail [15,20]. Then, the flow stress of the MLS, σ_{MLS}, at any given ε can be written in terms of the flow stresses of the constituents,σ_{301} and σ_{420} as:

$$\sigma_{\mathrm{MLS}}(\varepsilon) = f_{301}\sigma_{301}(\varepsilon) + (1 - f_{301})\sigma_{420}(\varepsilon) \quad (1)$$

where f denotes the volume fraction, and subscripts MLS and 301 and 420 indicate to the respective materials. If σ_{301} and σ_{420} data are available, it would then be possible to critically examine whether or not the simple rule of mixtures relation given in Eq. (1) holds. Ideally, one should obtain such data from uniaxial tensile tests performed on the constituent materials. However, if they are evaluated on the bulk materials, they may not truly represent those of the constituent layers for the following two reasons. (i) The layers are considerably thin and hence may be much stronger than the bulk, i.e., there could be a size effect. (ii) The layers are subjected to thermomechanical processes during the manufacturing of the MLS. This process history could potentially make the mechanical response vastly different from those of the bulk samples. One alternative is to extract the layers from the MLS and then test them. Since both the layers are metallic in nature and the interface is not well defined, separating them into thin strips is a difficult proposition. Even if one is successful in extracting the individual layers, tensile testing such thin layers is not a straight forward task. Therefore, we have resorted to spherical nanoindentation on the layers, to extract their properties. Representative load-displacement (P-h) curves obtained on the 301 and 420 layers are displayed in Fig. 3a. The maximum displacement at the peak load ($h_{\max}$) is larger for 301 layer than for 420 layer, which indicates that the latter is harder than the former.

Since Tabor's pioneering work in the middle of 1940s [21], a substantial amount of effort has been made to pursue the relationship between the data acquired from spherical indentation experiments and the macroscopic flow stress-strain behavior of metallic and ceramic materials. Many ideas and concepts on this issue have been developed over the several past decades, and now it is generally accepted (e.g., see for example [12,15,22–33]) that the uniaxial stress-strain curve can be (at least, roughly) extracted by instrumented indentation with a spherical tip. This is mainly thanks to the absence of "geometrical self-similarity" in spherical indentation. In an indentation using a sharp tip (which is geometrically self-similar), unique (or so-called representative) stress and strain underneath the indenter can be defined irrespective of indentation load. However, during a spherical indentation, the stresses and strains increase with load (and thus penetration depth) as the flow stress and strain do in uniaxial tension. The representative flow stress, σ_{Re}, can be estimated from the nanoindentation data by using the well-known Tabor's empirical relationship, $\sigma_{\mathrm{Re}} = \frac{H}{C} = \frac{P}{\pi a^2 C}$ [21], where H is the hardness (that is equal to the mean contact pressure p_m), C is the constraint factor (~3 for fully plastic deformation [34]), P is the indentation load, and a is the contact radius. The characteristic strain underneath a spherical indenter is often described as $\varepsilon_{Ch} = 0.2\frac{a}{R}$ [21]. Therefore, σ_{Re} and ε_{Ch} can be determined when the value of a is estimated from the knowledge of the contact depth, h_c (given by $h_c = h - \omega\frac{P}{S}$

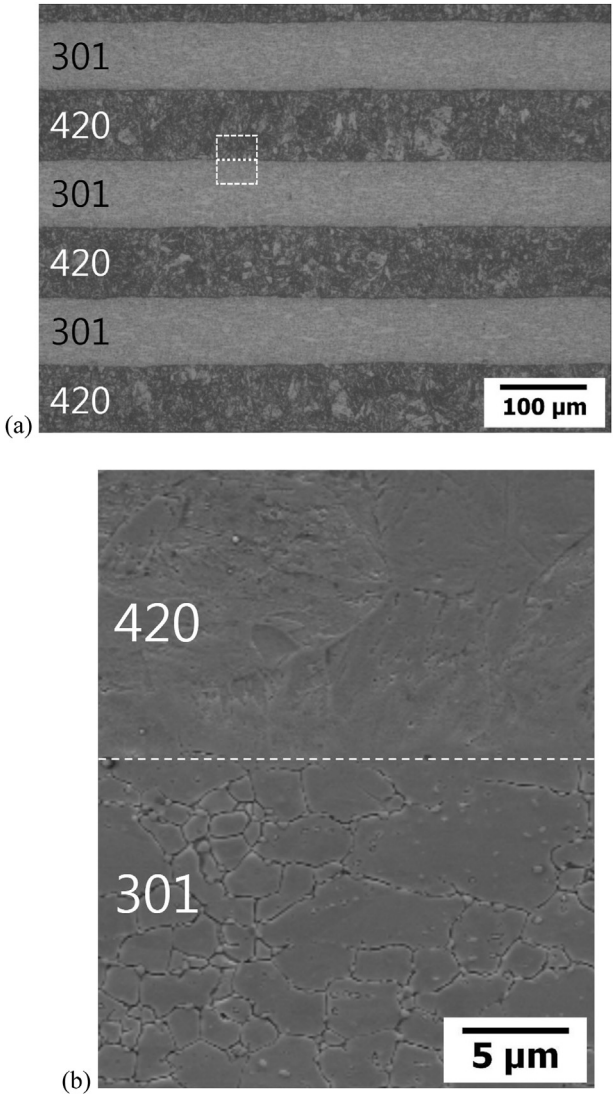

Fig. 1. Composite structures of the produced MLS; (a) optical micrographs showing typical microstructure; (b) SEM image magnifying the near-interface region that is marked in (a).

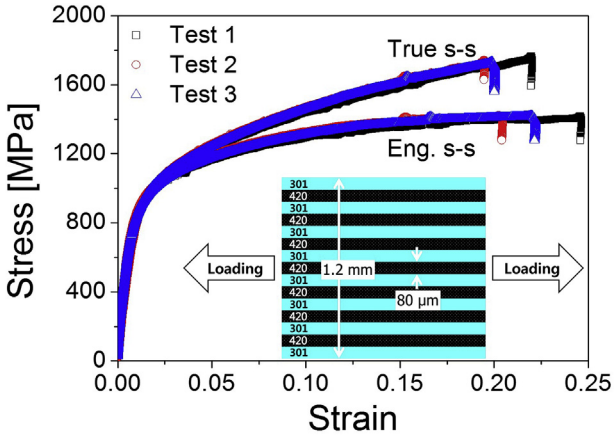

Fig. 2. Tensile stress-strain responses of MLS (with inset showing schematic of MLS structure and designed loading direction).

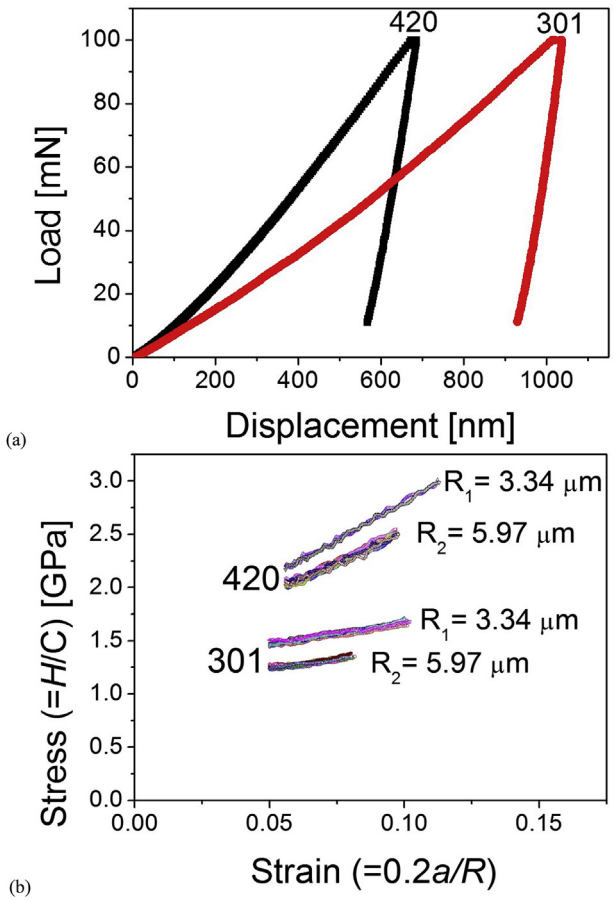

Fig. 3. Representative examples of spherical indentation data; (a) *P-h* curves of both 420 and 301 layers (for $R = 3.34$ μm); (b) σ-ε relations converted from nanoindentation data of each layer.

[35,36] where S is the contact stiffness and ω is a geometric constant; 0.75 for a sphere) and the contact geometry equation: $a^2 = 2Rh_c - h_c^2$ [12,15].

Fig. 3b shows the plots of σ_{Re} vs. ε_{Ch} estimated according to the above procedure. Here, we ignored the data points from the early stage of contact, due to large fluctuations in them. The following three observations can be made from Fig. 3b. (i) As expected from Fig. 3a, for both tips of $R = 3.34$ and 5.97 μm, 420 exhibits higher σ_{Re} than 301. (ii) For any layer and tip combination, σ_{Re} increases with ε_{Ch}. (iii) For both the layers, the σ_{Re} values for smaller R (3.34 μm) are higher than those obtained with a larger R (5.97 μm).

The σ_{Re} vs. ε_{Ch} plots in Fig. 3b cannot be directly compared to the macroscopic σ-ε curves obtained from the standard tensile tests of bulk MLS samples (shown in Fig. 2) because of the indentation size effect (ISE) on H (and thus σ_{Re}). Hence, the H data needs to be corrected for ISE first. The ISE for spherical indentation is different from that for sharp indentation; H strongly depends on R rather than h in the former [37,38] as per the following relation that was experimentally verified by Swadener et al. [38]:

$$H = H_0\sqrt{1 + \frac{R^*}{R}} \tag{2}$$

where H_0 is the macroscopic hardness and R^* is the material length scale for the R dependence of H. From the calculated H_0 of each layer, macroscopic flow stresses of each layer [i.e., σ_{301} and σ_{420} of Eq. (1)] at a given ε can be estimated. By extrapolating the σ_{Re} values for a reasonably large R (500 μm [12,15]) according to Eq. (2), the macroscopic σ-ε data of each layer could be derived as exhibited in Fig. 4.

Since the full range of σ-ε data cannot be estimated by the above procedure, it is needed to extrapolate the estimated σ_{Re} (for R ~ 500 μm) to a wider range by fitting the data according to an appropriate law for describing the strain hardening within the plastic flow regime. Based on the experimentally measured flow curves for martensitic and austenitic stainless steels in the literature [7,20,39–41], the Hollomon power law, $\sigma = K\varepsilon^n$ (where K is the strength coefficient and n is the work-hardening exponent) [42], was used for 420 layer [7,20] while a linear-hardening-type equation, $\sigma = X\varepsilon + Y$ (where X is the slope and Y is the y-intercept of the fitting line), was adopted for 301 layer [7,39–41]. The σ-ε relation within the elastic regime was assumed to follow Hooke's law: $\sigma = E\varepsilon$ (with a general E value of steel, ~200 GPa) and the yield strain was simply determined as the crossing point of the fitting curves and the line of Hooke's law. From this, the macroscopic σ-ε relations for the 301 and 420 layers were determined as σ_{301} (in MPa) $= 1447\cdot\varepsilon + 784$ and σ_{420} (in MPa) $= 2544\cdot\varepsilon^{0.12}$, respectively.

From the σ-ε relations of each layer, the macroscopic flow curve of the MLS was predicted by using Eq. (1). Fig. 5 compares the predicted and the representative experimental σ-ε curves. A reasonably good agreement between the two indicates that the each constituent layer contributes nearly equally – and as per the rule of mixtures – to the global strength of MLS. It is noteworthy that, in the case of 420, actual tensile failure of the monolithic sample occurs at very early ε of the dashed curve of 420 in Fig. 5 (e.g., <5% [7]).

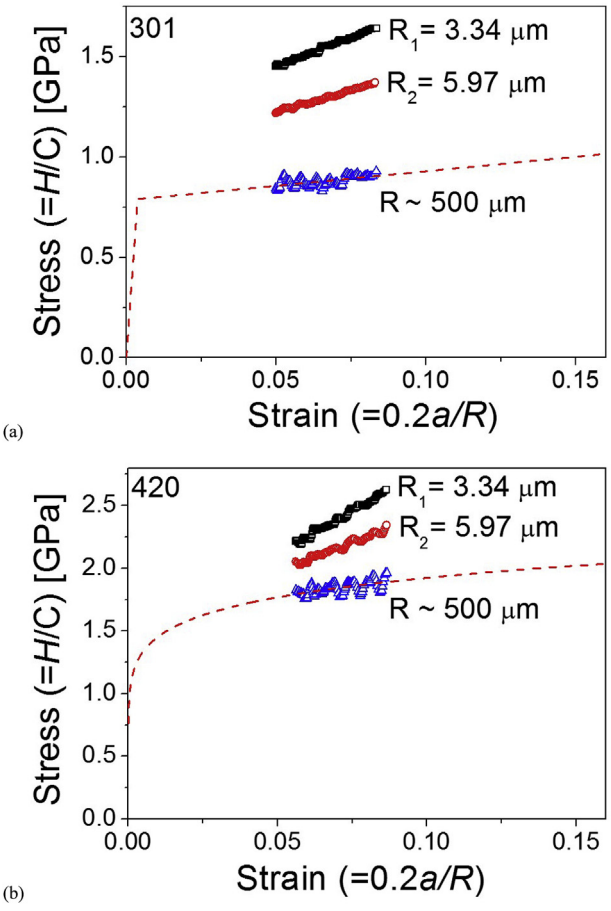

Fig. 4. Estimated macroscopic flow behavior of each layer; (a) 301 and (b) 420 layer.

A slight difference between the measured and the predicted responses may be primarily due to the iso-strain assumption. Although it is a reasonable assumption for the tensile loading condition of MLS (see Fig. 2), two-types of strain partitioning in the MLS can be envisioned: macroscopic partitioning of strain between the two different constituent layers, and microscopic strain inhomogeneity within each layer, especially in the ductile 301 layer. To evaluate the former, finite element (FE) simulations were performed by using the ABAQUS software (HKS Inc., Pawtucket, RI). For the sake of simplicity, only a five-layer structure (in the sequence of 301-420-301-420-301with an initial layer thickness of 0.8 mm) and a hard contact between the layers were assumed. A dog-bone shaped specimen with a 14,560 element mesh was generated. A total displacement of 25 mm (corresponding to ε ~ 0.32) was applied to the sample. The material parameters used for the simulations were based on the flow curve of each layer estimated from the nanoindentation data.

Results of the FE simulations are shown in Fig. 6a where the distribution of the average equivalent plastic strains, $\overline{\varepsilon_p}$, within the five-layered specimen is illustrated. In Fig. 6b, the distributions of $\overline{\varepsilon_p}$ in 301 and 420 layers are compared. As expected, larger plastic strains are observed in the softer 301 layer than in the 420 layer. Similar results were obtained by Paul and Mukherjee [20], who also performed FE simulations, reported the larger strains of soft ferrite than hard martensite layers within the MLS under similar loading conditions as that in Fig. 2.

Another possible reason for the difference between the predicted and experimental stress-strain responses displayed in Fig. 5 is the fact that only two spherical tips were used in the present study for estimating the tensile behavior from the nanoindentation responses. Using only two tips always results in a linear relation between H (and σ_{Re}) and R^2 (of Eq. (2)) so that the extrapolated σ_{Re} for R ~ 500 μm can be significantly affected by a small fluctuation in H of each tip. Therefore, the use of more number of tips having different R will certainly enhance the accuracy of the predictions.

Before closing this section, it is important to recall that in Fig. 5 the hardening behavior of MLS is different from that of either of the 420 or 301 layer, which is indeed one of the main objectives of "multi-layering." Two possible explanations for the observed difference are the presence of interfaces and the existence of neighboring layers (resulting in the change in mechanical environment in terms of constraint offered for deformation). It is reasonable to expect that both of them can affect the hardening behavior and alter it from that of monolithic sample of each layer, although further study for quantitative analysis of this is required.

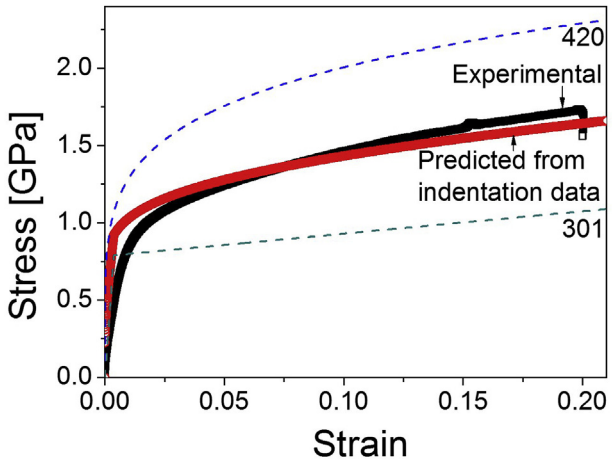

Fig. 5. Comparison of the flow curve predicted from nanoindentation analysis to that measured from standard tensile test of MLS.

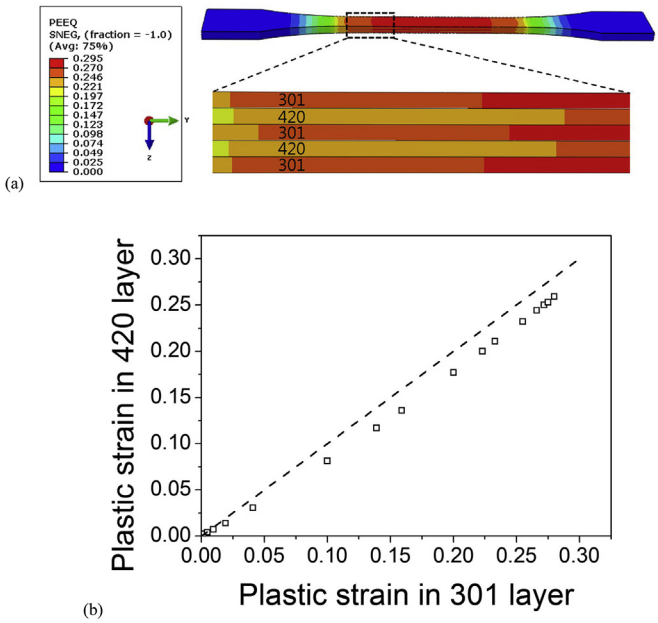

Fig. 6. FE simulation of macroscopic strain partitioning in five-layer steel; (a) the distribution of equivalent plastic strain and (b) the average plastic strain of 301 and 420 layers.

4. Ductility

Although the analysis performed in the above section informs us about the role of constituent's strength on the overall strength of MLS, it does not provide any insight as to how the global tensile ductility (i.e., failure strain ε_f) of the MLS is determined. In particular, a large difference in ε_f of monolithic 420 and 301 samples (i.e., the former exhibits much smaller ε_f than the latter [7,43]) exists. Therefore, a simple rule-of-mixture type approach cannot be used for estimating the contribution of each layer to ε_f. In addition, spherical nanoindentation experiments cannot produce any data related to ε_f. Keeping this in mind, we attempt to indirectly examine the roles of the constituent layers in determining the ε_f of MLS through nanoindentation hardness, H, measurements of each layer, as following.

Since the global ε_f of examined MLS approaches 20% (see Fig. 5), five different samples experiencing different level of ε (0, 5, 10, 15%, and ε_f ~ 20%) are prepared by interrupted tensile tests. The true stress vs. true strain curves obtained from the tensile tests interrupted at different ε are shown in Fig. 7a, in which overlapping of all curves proves a good reproducibility of σ-ε relation of this MLS. Subsequently, a series of nanoindentation experiments with a Berkovich indenter were performed on each of the 420 and 301 layer in the five samples. Fig. 7b shows the typical P-h curves obtained from unstrained specimen ($\varepsilon = 0$), with the inset SEM images being the representative indentation impressions made on 301 and 420 layers. From the P-h curves, the H values of each layer were estimated by the Oliver-Pharr method [35,36]. Fig. 7c shows the variation in the H values of both layers as a function of the applied ε. It is seen that while the H of 301 layer increases continuously with ε, the H of 420 layer is almost constant and independent of ε after an initial slight increases until ε of 5%. The latter observation implies that there is almost negligible strain hardening in the 420 layer. Since the tensile response of this MLS

exhibits marked strain hardening and the flow response of 420 layer is ε-independent, it is reasonable to conclude that macroscopic strain hardening of the MLS is due to the work hardening in the 301 layers.

We note that the variation in the hardness of each layer in Fig. 7c cannot be directly compared with the predicted flow behavior of each layer in Fig. 5. The predicted curves in Fig. 5 were extracted from spherical indentation on each layer of "un-deformed" MLS. Since impression areas were so small and thus interface effects can be ignored, the predicted curves in Fig. 5 represent those for the monolithic 301 and 420 samples (that have no influence of neighboring layers). On the contrary, the hardness values in Fig. 7c were obtained from nanoindentation on each layer of "deformed" MLS, and thus the hardness change is corresponding to the macroscopic straining of MLS. As shown in Fig. 5, the hardening behavior of such monolithic (either 301 or 420) sample is different from the macroscopic behavior of MLS, and thus they cannot be directly compared with each other.

An interesting feature in Fig. 7c is that the failure of tensile specimen occurred when the H of the 301 layer becomes similar to the H value of the 420 layer. As shown in Fig. 6a, the 301 layers accommodate a large amount of plastic deformation, which starts while the 420 layer is still elastic. This large plasticity can lead to the strain-induced martensitic phase transformation (SIMPT) that is well known to occur in austenitic stainless steels. In view of this, the origins of the work hardening observed in the 301 layer may also have roots in the occurrence of SIMPT, which converts the softer austenitic phase into a harder martensitic phase. This is in addition to that caused by an increase in the dislocation density due to the plastic deformation. Based on this possibility and the fact that the monolithic 420 has a much smaller ε_f than 301, one can expect that the tensile failure of the MLS may occur at the ε where a large portion of the 301 layers have undergone SIMPT. This possibility is supported by the observation of near-equal H in both the layers at the global ε_f of the MLS.

To further verify this scenario, SIMPT in the top 301 layer was investigated by employing the magnetic method as well as and XRD. First, by using Feritscope, the martensite volume fraction (f_M) on the surface of the top layer was estimated macroscopically. In these experiments, a low-frequency alternating magnetic field is generated around a cylindrical-shaped iron probe (5 mm in

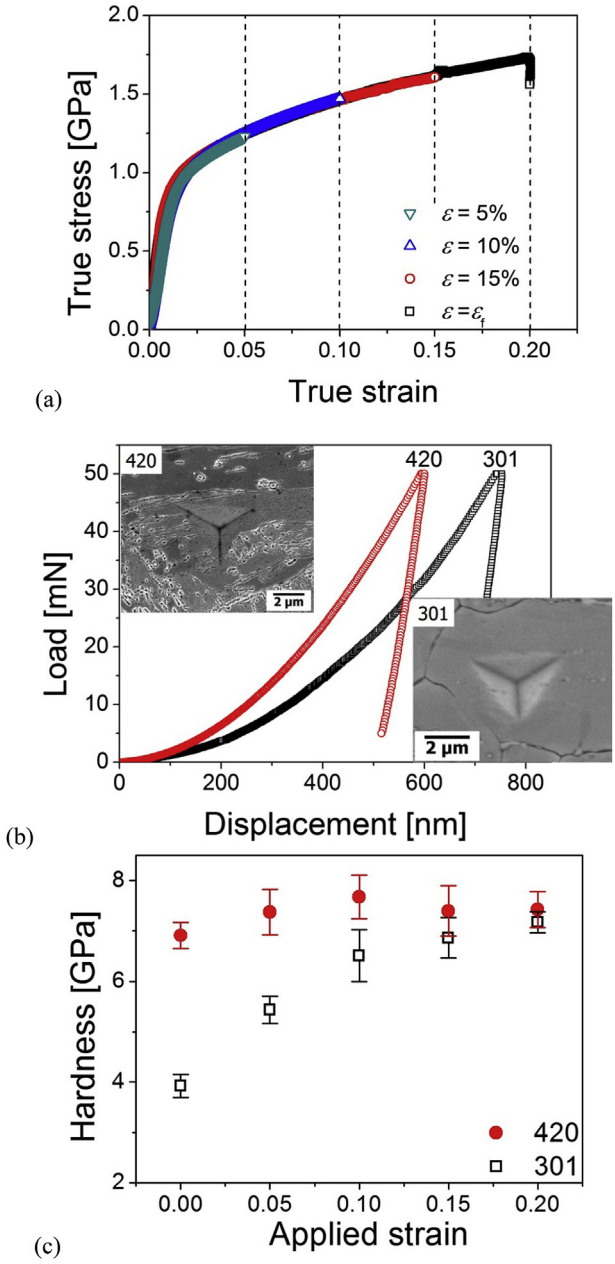

Fig. 7. Nanoindentation results of interrupted tensile specimens; (a) plots of true stress vs. true strain obtained from interrupted tensile tests; (b) example of nano-indentation P-h curves (for as-received sample) with an inset SEM image showing hardness impressions; (c) changes in hardness of each layer with the applied tensile strain.

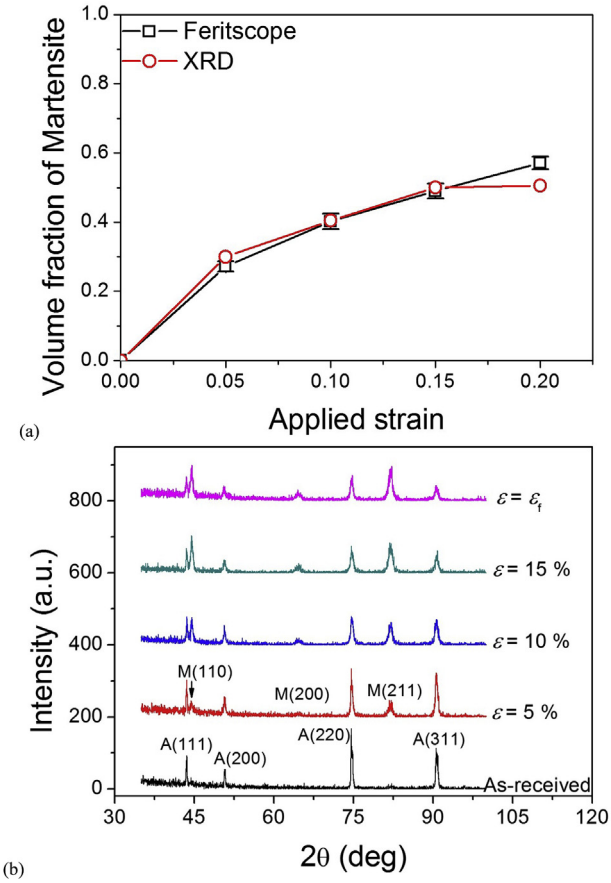

Fig. 8. Measurements of martensite fraction in the top 301 layer; (a) martensite fractions measured from Feritscope and XRD; (b) typical XRD patterns of both as-received and deformed specimens.

diameter), and the change in the surrounding magnetic field is measured using a coil wound around the probe. From the magnetic permeability measurement, the martensite content could be estimated in a manner analogous to that for the ferrite content estimation that is routinely employed in ferrous industries [44]. The raw data obtained by the instrument were multiplied by a correction factor of 1.7 for f_M, following the method introduced in Ref. [18]. The estimated f_M values are summarized as a function of the applied ε in Fig. 8a. We note from it that f_M increases significantly with ε.

In the second method, XRD analysis was employed to examine the variation of f_M with ε. Fig. 8b shows the obtained XRD peaks. Note that before tensile testing, there are only austenite peaks (<111>, <200>, <220>, and <311>) in the range of 2θ from 30° to 100°. From XRD data, f_M was determined with Material Analysis Using Diffraction (MAUD) software (University of Trento, Italy) and the results are also summarized in Fig. 8a. The results from both methods are in a good agreement for the entire range of ε examined in this study. It is interesting to note from Fig. 8a that at the global ε_f of MLS (~20%), the estimated f_M is only ~ 0.5–0.6 while H of 301 layer approaches the same level as that of 420 layer (see Fig. 7c). This may be because the top 301 layer experiences relatively less constraint of mechanical environment vis-a-vis those in the interior of the MLS.

In order to investigate the change in f_M in the interior layers, cross-sectional EBSD analysis was conducted on the layer located at the mid-thickness. In Fig. 9, the EBSD phase mapping images obtained on it at different applied ε are shown. For a better identification of the interfaces, the corresponding IQ map images were displayed in the insets. The color scheme employed is such that red is austenite while green is martensite. The inter-layer interfaces are indicated with dashed lines. From these images, it is obvious that the f_M of the mid-thickness 301 layer increases with ε; f_M ~0.29, 0.47, 0.74, and 0.8 for ε ~5, 10, 15%, and ε_f (~20%), respectively. Also, f_M in layers inside the sample is larger than that estimated for the top layer. The difference between these two f_M values (Δf_M) at a given ε becomes larger with ε, i.e., Δf_M ~ 0.01, 0.07, 0.24, and 0.26 at ε ~ 5, 10, 15%, and ε_f (~20%), respectively. Since this differential strain has to be accommodated by the neighboring 420 layers, we can surmise that they will have an important role to play in the martensitic transformation.

In Fig. 10, the variation in f_M with ε obtained in the present study is compared with the f_M data from standard tensile tests of monolithic 301 samples reported in Ref. [41]. The ε_f of the monolithic 301 sample [41] (~55%) is much higher than that of MLS (~20%). Considering the observation that ε_f of the MLS is almost the same as the ε where H of the 301 layer reaches that of 420 layer, Fig. 10 suggests again that the existence of the neighboring 420 layers enhances the martensitic transformation. This is additionally supported by a couple of intriguing features observed in Fig. 10; at ε_f of MLS (~20%), the value of f_M for mid-thickness layer (~0.8) is considerably higher than that observed in the monolithic 301 specimen (~0.3). Also, the f_M of monolithic 301 sample at its ε_f is close to the f_M of mid-thickness 301 layer at ε_f of MLS.

From Fig. 9, one can gauge the important role played by the 420 layers in the martensitic transformation in the 301 layers. The transformation occurs preferentially near the interfaces at a relatively small ε, and then proceeds into the center of the layer. At $\varepsilon = \varepsilon_f$, most of the 301 layer is transformed into martensite (f_M ~ 0.8). This is further exemplified in Fig. 11, which shows the

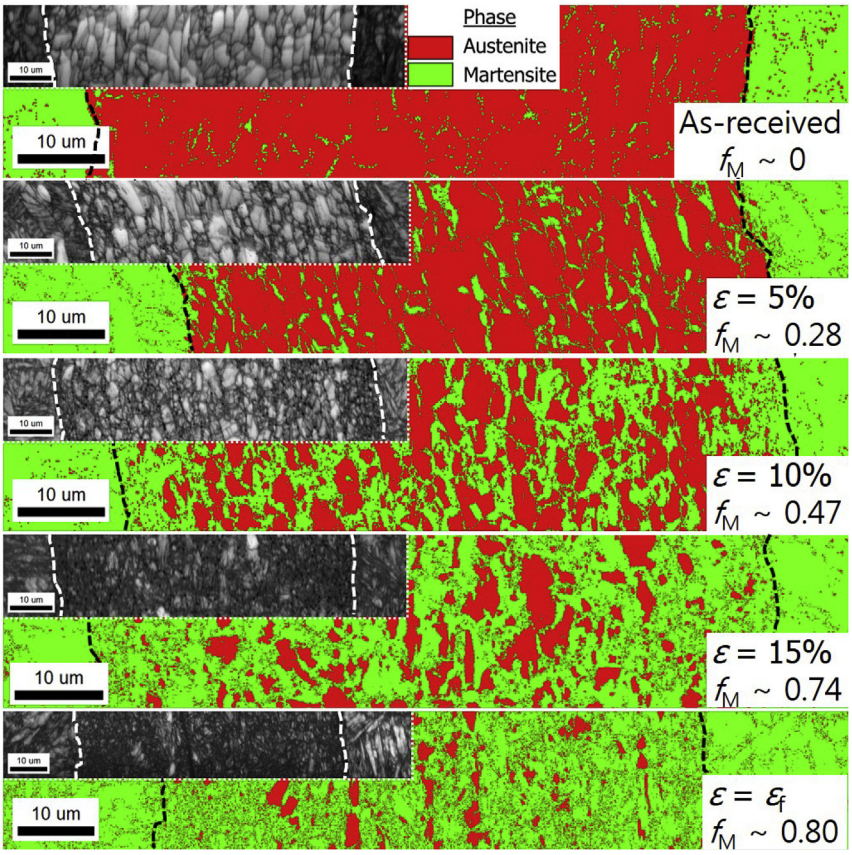

Fig. 9. EBSD phase mapping images showing the changes in martensite volume fraction in mid-thickness 301 layer. Inset images are corresponding IQ maps taken to clarify inter-layer interfaces.

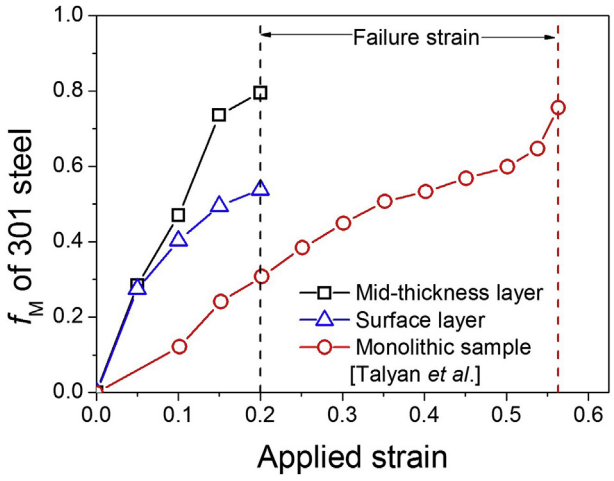

Fig. 10. Comparison of martensite volume fractions in 301 layers of MLS to the literature data of monolithic 301 sample [41].

distribution of the austenite volume fraction, f_A, as a function of the distance from the interlayer interface. The f_A near the interfaces is smaller than in the center of layer, suggesting the transformation

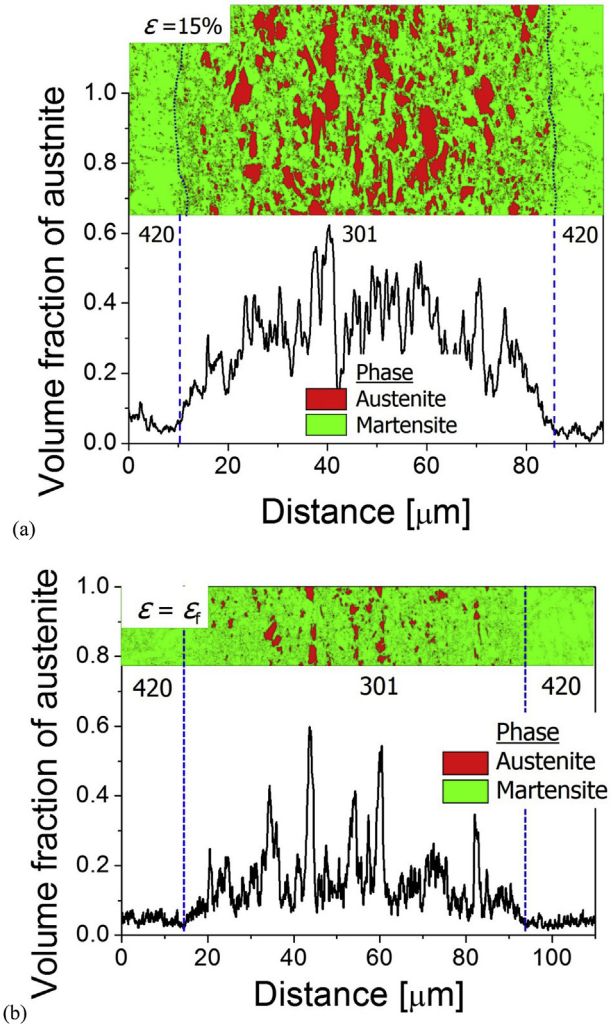

Fig. 11. Distributions of the austenite volume fraction within 301 layer; (a) ε = 15 and (b) 20%.

occurs preferentially in the region near the interfaces. A possible reason for this phenomenon is the existence of steeper strain gradient near the interfaces. Recent two dimensional representative volume element (RVE) FE simulations of DP steels [45–47] show that the equivalent plastic strain of the soft phase matrix is much higher in the region near the phase boundaries than in the center region. Similar behavior is expected to occur in the MLS examined in this study, and such high strain (and strain energy) can directly enhance the SIMPT near the interfaces. Another possibility is related to the concept of geometrically necessary dislocations (GNDs) associated with steep strain gradients. Such gradients, present near the interfaces, mandate a higher density of GNDs in the austenite grains that are located in the region [8]. Ramazani et al. [47] reported that in a DP steel, the level of equivalent plastic strain in the soft phase decreases from the distance from the interface and that the GND zone in the soft phase is developed near the interfaces. Since dislocations are well known to lower the barrier for SIMPT (either by their movement or by their elastic strain field) [48], the increased GND density near the interfaces conceivably enhances the martensitic transformation. This scenario is consistent with the experimental results and may successfully explain why SIMPT starts preferentially in the 301 grains near the interfaces.

5. Conclusions and outlook

In the present study, the contributions of the constituent austenite and martensite layer materials to the macroscopic tensile responses of a recently developed hybrid steel that consists of alternating layers of 301 austenitic stainless steel and 420 martensitic stainless steel, was investigated through a series of nanoindentation experiments, which are complemented with microstructural and finite element analyses. The following are the key conclusions of this investigation.

The macroscopic tensile flow response of the MLS can be predicted reasonably well with the knowledge of the flow responses of the constituent layers, which were estimated by employing spherical nanoindentation tests with different tip radii, and applying simple rule of mixtures. The strain hardening observed in the MLS is mainly due to that in the 301 layer, which has origins in both work hardening as well as the strain-induced austenite-to-martensite phase transformation. The observation that the failure strain of the MLS corresponds to the strain at which the flow resistances of both phases are equal, suggests that the tensile ductility of the MLS is controlled by the phase transformation in the austenite layers as well as the mechanical environment change imposed by the martensite layers.

The above conclusions offer us some avenues for the possible design of MLS with even better properties. The fact that the rule of mixtures is obeyed for strength suggests that further enhancements in strength can be obtained by either incorporating even stronger constituents or by increasing the martensite content, or both. In such a case, one has to ensure that the ductility is not compromised for the sake of enhancing the strength. In that context, results of the present study show that the change in mechanical environment offered by the harder martensite phase to the phase transformation in the austenite layers holds the key. Therefore, playing with the architecture of the layers in terms of controlling their thickness (and the portion of interfaces) holds further promise.

Acknowledgements

This work was supported in part by the National Research Foundation of Korea (NRF) grant funded by the Korea government

(MSIP) (No. NRF-2013R1A1A2A10058551), and in part by the NRF grant funded by the MSIP (No. NRF-2015R1A5A1037627).

References

[1] T. Koseki, J. Inoue, S. Nambu, Development of multilayer steels for improved combinations of high strength and high ductility, Mater. Trans. 55 (2014) 227–237.

[2] J. Inoue, S. Nambu, Y. Ishimoto, T. Koseki, Fracture elongation of brittle/ductile multilayered steel composites with a strong interface, Scr. Mater. 59 (2008) 1055–1058.

[3] J. Yanagimoto, T. Oya, S. Kawanishi, N. Tiesler, T. Koseki, Enhancement of bending formability of brittle sheet metal in multilayer metallic sheets, CIRP Ann-Manuf. Technol. 59 (2010) 287–290.

[4] D.R. Lesuer, C.K. Syn, O.D. Sherby, J. Wadsworth, J.J. Lewandowski, W.H. Hunt, Mechanical behavior of laminated metal composites, Int. Mater. Rev. 41 (1996) 169–197.

[5] C.K. Syn, D.R. Lesuer, J. Wolfenstine, O.D. Sherby, Layer thickness effect on ductile tensile fracture of ultrahigh carbon steel-brass laminates, Metall. Trans. A 24 (1993) 1647–1653.

[6] S. Nambu, M. Michiuchi, J. Inoue, T. Koseki, Effect of interfacial bonding strength on tensile ductility of multilayered steel composites, Compos. Sci. Technol. 69 (2009) 1936–1941.

[7] P. Lhuissier, J. Inoue, T. Koseki, Strain field in a brittle/ductile multilayered steel composite, Scr. Mater. 64 (2011) 970–973.

[8] R.I. Barabash, O.M. Barabash, M. Ojima, Z. Yu, J. Inoue, S. Nambu, T. Koseki, R. Xu, Z. Feng, Interphase strain gradients in multilayered steel composite from microdiffraction, Metal. Mater. Trans. A 45A (2014) 98–108.

[9] M. Ojima, J. Inoue, S. Nambu, P. Xu, K. Akita, H. Suzuki, T. Koseki, Stress partitioning behavior of multilayered steels during tensile deformation measured by in situ neutron diffraction, Scr. Mater. 66 (2012) 139–142.

[10] M. Ojima, Y. Adachi, Y. Tomota, K. Ikeda, T. Kamiyama, Y. Katada, Work hardening mechanism in high nitrogen austenitic steel studied by in situ neutron diffraction and in situ electron backscattering diffraction, Mater. Sci. Eng. A 529 (2009) 16–24.

[11] J. Moon, S. Kim, J.-i. Jang, J. Lee, C. Lee, Orowan strengthening effect on the nanoindentaion hardness of ferrite matrix in microalloyed steels, Mater. Sci. Eng. A 487 (2008) 552–557.

[12] B.-W. Choi, D.-H. Seo, J.-Y. Yoo, J.-i. Jang, Predicting macroscopic plastic flow of high-performance, dual-phase steel through spherical nanoindentation on each micro phase, J. Mater. Res. 24 (2009) 816–822.

[13] B.-W. Choi, D.-H. Seo, J.-Y. Yoo, J.-i. Jang, A nanoindentation study on the micromechanical characteristics of API X100 pipeline steel, Met. Mater. Int. 15 (2009) 373–378.

[14] S. Kang, Y.-S. Jung, B.-G. Yoo, J.-i. Jang, Y.-K. Lee, Orientation-dependent indentation modulus and yielding in a high Mn twinning-induced plasticity steel, Mater. Sci. Eng. A 532 (2012) 500–504.

[15] M.-Y. Seok, Y.-J. Kim, I.-C. Choi, Y. Zhao, J.-i. Jang, Predicting flow curves of two-phase steels from spherical nanoindentation data of constituent phases: iso-strain method vs. non-isostrain method, Int. J. Plast. 59 (2014) 108–118.

[16] M.-Y. Seok, I.-C. Choi, J. Moon, S. Kim, U. Ramamurty, J.-i. Jang, Estimation of the Hall–Petch strengthening coefficient of steels through nanoindentation, Scr. Mater. 87 (2014) 49–52.

[17] H. Hertz, J. Reine Angew. Math. 92 (1881) 156. Translated and reprinted in English in "Hertz's Miscellaneous Papers" edited by D.E. Jones, G.H. Schott, Macmillan& co, London, 1896 Ch. 5.

[18] J. Talonen, P. Aspegren, H. Hanninen, Comparison of different methods for measuring strain induced α'-martensite content in austenitic steels, Mater. Sci. Technol. 20 (2004) 1506–1512.

[19] Y.-J. Kim, B.-G. Yoo, I.-C. Choi, M.-Y. Seok, J.-Y. Kim, T. Ohmura, J.-i. Jang, Martensitic phase transformation and pop-in in compression of austenitic steel nanoplates observed in situ by transmission electron microscopy, Mater. Lett. 75 (2012) 107–110.

[20] S.K. Paul, M. Mukherjee, Determination of bulk flow properties of a material from the flow properties of its constituent phases, Comp. Mater. Sci. 84 (2014) 1–12.

[21] D. Tabor, Hardness of Metals, Clarendon Press, Oxford, 1951.

[22] J.S. Field, M.V. Swain, Determining the mechanical properties of small volumes of material from submicrometer spherical indentations, J. Mater. Res. 10 (1995) 101–112.

[23] J.S. Field, M.V. Swain, The indentation characterisation of the mechanical properties of various carbon materials: glassy carbon, coke and pyrolytic graphite, Carbon 34 (1996) 1357–1366.

[24] Y.Y. Lim, A.J. Bushby, M.M. Chaudhri, Nano and macro indentation studies of polycrystalline copper using spherical indenters, Mat. Res. Soc. Symp. Proc. 522 (1998) 145–150.

[25] N. Huber, Ch Tsakmakis, Determination of constitutive properties from spherical indentation data using neurl networks. Part I, J. Mech. Phys. Solids 47 (1999) 1569–1588.

[26] D. Ma, C.W. Ong, J. Lu, J. He, Methodology for the evaluation of yield strength and hardening behavior of metallic materials by indentation with spherical tip, J. Appl. Phys. 94 (2003) 288–294.

[27] Y.J. Park, G.M. Pharr, Nanoindentation with spherical indenters: finite element studies of deformation in the elastic-plastic transition regime, Thin Solid Films 447–448 (2004) 246–250.

[28] Y.P. Cao, J. Lu, A new method to extract the plastic properties of metal materials from an instrumented spherical indentation loading curve, Acta Mater. 52 (2004) 4023–4032.

[29] J.-i. Jang, Y. Choi, Y.-H. Lee, J.-S. Lee, D. Kwon, M. Gao, R. Kania, Application of instrumented indentation technique for enhanced fitness-for-service assessment of pipeline crack, Int. J. Fract. 131 (2005) 15–34.

[30] E.G. Herbert, W.C. Oliver, G.M. Pharr, On the measurement of yield strength by spherical indentation, Phil. Mag. 86 (2006) 5521–5539.

[31] S. Basu, A. Moseson, M.W. Barsoum, On the determination of spherical nanoindentation stress-strain curves, J. Mater. Res. 21 (2006) 2628–2637.

[32] U. Ramamurty, J.-i. Jang, Nanoindentation for probing the mechanical behavior of molecular crystals-a review of the technique and how to use it, Cryst. Eng. Comm. 16 (2014) 12–23.

[33] S. Pathak, S.R. Kalidindi, Spherical nanoindentation stress-strain curves, Mater. Sci. Eng. Rep. 91 (2015) 1–36.

[34] S. Shim, J.-i. Jang, G.M. Pharr, Extraction of flow properties of single crystal silicon carbide by nanoindentation and finite element simulation, Acta Mater. 56 (2008) 3824–3832.

[35] W.C. Oliver, G.M. Pharr, An improved technique for determining hardness and elastic modulus using load and displacement sensing indentation experiments, J. Mater. Res. 7 (1992) 1564–1583.

[36] W.C. Oliver, G.M. Pharr, Measurement of hardness and elastic modulus by instrumented indentation: advances in understanding and refinements to methodology, J. Mater. Res. 19 (2004) 3–20.

[37] G.M. Pharr, E.G. Herbert, Y. Gao, The indentation size effect: a critical examination of experimental observations and mechanistic interpretations, Annu. Rev. Mater. Res. 40 (2010) 271–292.

[38] J.G. Swadener, B. Taljat, G.M. Pharr, Measurement of residual stress by load and depth-sensing indentation with spherical indenters, J. Mater. Res. 16 (2001) 2091–2102.

[39] Y.F. Shen, X.X. Li, X. Sun, Y.D. Wang, L. Zuo, Twinning and martensite in a 304 austenitic stainless steel, Mater. Sci. Eng. A 552 (2012) 514–522.

[40] A.G. Pineau, R.M. Pelloux, Influence of strain-induced martensitic transformations on fatigue crack growth rates in stainless steels, Metal. Trans. 5 (1974) 1103–1112.

[41] V. Talyan, R.H. Wagoner, J.K. Lee, Formability of stainless steel, Metal. Mater. Trans. A 29A (1998) 2161–2172.

[42] J.H. Hollomon, Tensile deformation, Trans. Am. Inst. Min. Metall. Eng. 162 (1945) 268–290.

[43] S. Nambu, M. Michiuchi, Y. Ishimoto, K. Asakura, J. Inoue, T. Koseki, Transition in deformation behavior of martensitic steel during large deformation under uniaxial tensile loading, Scr. Mater. 60 (2009) 221–224.

[44] A.M. Beese, D. Mohr, Effect of stress triaxiality and Lode angle on the kinetics of strain-induced austenite-to-martensite transformation, Acta Mater. 59 (2011) 2589–2600.

[45] S.K. Paul, A. Kumar, Micromechanics based modeling to predict flow behavior and plastic strain localization of dual phase steels, Comp. Mater. Sci. 62 (2012) 66–74.

[46] S.K. Paul, Real microstructure based micromechanical model to simulate microstructural level deformation behavior and failure initiation in DP 590 steel, Mater. Des. 44 (2013) 397–406.

[47] A. Ramazani, K. Mukherjee, A. Schwedt, P. Goravanchi, U. Prahl, W. Bleck, Quantification of the effect of transformation-induced geometrically necessary dislocations on the flow-curve modelling of dual-phase steels, Int. J. Plast. 43 (2013) 128–152.

[48] D.A. Porter, K.E. Easterling, M.Y. Sherif, Phase Transformations in Metals and Alloys, Third Edition, CRC press, FL, 2009.